Journal of Catalysis 269 (2010) 53–63

Contents lists available at ScienceDirect

Journal of Catalysis

journal homepage: www.elsevier.com/locate/jcat

DFT study of nitrided zeolites: Mechanism of nitrogen substitution in HY and silicalite

Vishal Agarwal [a], George W. Huber [a], W. Curtis Conner Jr. [a], Scott M. Auerbach [a,b,*]

[a] Department of Chemical Engineering, University of Massachusetts, Amherst, MA 01003, USA
[b] Department of Chemistry, University of Massachusetts, Amherst, MA 01003, USA

ARTICLE INFO

Article history:
Received 21 July 2009
Revised 10 September 2009
Accepted 19 October 2009
Available online 9 December 2009

Keywords:
Nitrided zeolites
Solid base catalysts
Ammonolysis
Mechanism
Nudged elastic band
ONIOM
Density-functional theory

ABSTRACT

We have performed embedded-cluster calculations using density functional theory to investigate mechanisms of nitrogen substitution (nitridation) in HY and silicalite zeolites. We consider nitridation as replacing Si–O–Si and Si–OH–Al linkages with Si–NH–Si and Si–NH_2–Al, respectively. We predict that nitridation is much less endothermic in HY (29 kJ/mol) than in silicalite (132 kJ/mol), indicating the possibility of higher nitridation yields in HY. To reveal mechanistic details, we have combined for the first time the nudged elastic band method of finding elusive transition states, with the ONIOM method of treating embedded quantum clusters. We predict that nitridation of silicalite proceeds via a planar intermediate involving a $\equiv Si<^{N}_{O}>Si\equiv$ ring with pentavalent Si, whereas nitridation of HY is found to proceed via an intermediate similar to physisorbed ammonia. B3LYP/6-311G(d,p) calculations give an overall barrier for silicalite nitridation of 343 kJ/mol, while that in HY is 359 kJ/mol. Although the overall nitridation barriers are relatively high, requiring high temperatures for substitution, the overall barriers for the reverse processes are also high. As such, we predict that once these catalysts are made, they remain relatively stable.

1. Introduction

Zeolites are microporous crystalline materials with TO_4 (T = Si, Al) tetrahedra as primary units, joined via bridging oxygens to give cage-like structures [1]. Acidic zeolite catalysts have long been the backbone of the petroleum industry because of their high surface area, large adsorption capacities, and shape-selective properties. All these properties make them promising candidates for biofuel production catalysts. However, biomass is composed of heavily oxygenated compounds that will likely be more effectively activated by *basic* catalysts. Examples of base-catalyzed reactions important to biofuel processing include condensation reactions that form carbon–carbon bonds, trans-esterification of triglycerides giving bio-diesel, and esterification of organic acids making gasoline additives [2]. Unfortunately, because zeolites form strong acid sites, their base sites tend to be relatively weak. As such, a fundamental need in heterogeneous catalysis is the development of strong, shape-selective solid base catalysts. Effort has recently intensified in making strongly basic zeolites by nitridation, i.e., substituting Si–O–Si and Si–OH–Al linkages with Si–NH–Si and Si–NH_2–Al, respectively [3]. Although clear spectroscopic evidence of nitridation is just now emerging [4] after 40 years of research [5], the mechanism of nitridation has yet to be reported. In the present paper, we describe detailed density functional theory calculations revealing nitridation mechanisms in all-silica MFI zeolite (silicalite) and in acidic HY zeolite.

The first report of nitrided zeolites appeared in 1968 by Kerr and Shipman [5], who exposed HY to ammonia at elevated temperatures (>500 °C). Nitrogen was believed to enter the framework as a bridge between Al and Si atoms, though compelling evidence of this was not given. Since then various groups have applied ammono-thermal treatments to zeolites [4,6–14]. Some studies have reported that the resulting materials are active catalysts for reactions typically catalyzed by bases [8–10], such as the Knoevenagel condensation of benzaldehyde with malononitrile, suggesting that new basic sites have been formed by ammono-thermal treatment. However, the nature of the active sites and the resulting framework structure was largely unknown.

Quantum calculations on nitrided zeolites have been performed to investigate amine site stability [15,16], amine site base strength [16], and bifunctional acid–base properties [17–19]. Corma *et al.* performed quantum calculations on small clusters, and found that substituting Si–O–Si with Si–NH–Si is endothermic by ~100 kJ/mol, suggesting that high temperatures are needed for nitridation

* Corresponding author. Address: Goesmann 222, University of Massachusetts, Amherst, MA 01003-9336, USA. Fax: +1 413 545 4490.
E-mail addresses: vagarwal@ecs.umass.edu (V. Agarwal), huber@ecs.umass.edu (G.W. Huber), wconner@ecs.umass.edu (W.C. Conner Jr.), auerbach@chem.umass.edu (S.M. Auerbach).

0021-9517/$ - see front matter © 2009 Elsevier Inc. All rights reserved.
doi:10.1016/j.jcat.2009.10.015

[15]. Astala and Auerbach performed periodic DFT calculations on zeolites with small unit cells (SOD and LTA); they found that nitridation in all-silica zeolites introduces minimal strain because of the flexibility of surrounding Si–O–Si angles [16]. Their calculations also predict that the base strength of Si–NH–Si is nearly twice that of Si–O–Si; this was later confirmed by the CO_2 TPD studies of Han et al. [12]. Lesthaeghe et al. performed cluster calculations to investigate the properties of bifunctional acidic/basic zeolites with traditional Brønsted acid sites proximal to nitrided basic sites [17–19]. They found novel catalytic activity in such systems but only when the acid/base moieties are sufficiently removed to avoid auto-neutralization. All these calculations point to the very promising nature of nitrided zeolites, but still leave unclear what actually gets made by ammono-thermal treatment of zeolites, prompting intensified efforts at characterizing these materials.

Han et al. applied IR, Raman and ^{29}Si MAS NMR to zeolites exposed to alkylamines and heat, finding evidence of strong framework-amine interactions [12–14]. Recent ^{29}Si NMR of nitrided zeolites coupled with quantum chemical shift calculations provide unambiguous evidence, for the first time, that ammono-thermal treatment of HY zeolite yields resonances associated with Si–NH_2–Al linkages [4]. This finding underscores the ability of NMR—over other spectroscopies such as IR—to provide "smoking gun" evidence of nitridation in zeolites. This study also featured the use of quantum calculations to extract nitridation yields from the NMR spectra. Despite the promise of this breakthrough, the mechanism of such nitridation is still unclear. Discovering the mechanism(s) may explain observed nitridation rates, provide predictions of base catalyst stability, and shed light on the fundamental aspects of functionalizing zeolites. In the present paper, we investigate nitridation mechanisms using a novel synthesis of computational methods.

In siliceous zeolites, a reasonable nitridation mechanism involves the following two steps:

$$\equiv Si{-}O{-}Si\equiv + NH_3 \rightarrow \equiv Si{-}OH + H_2N{-}Si\equiv \ \text{(ammonolysis)},$$
$$\equiv Si{-}OH + H_2N{-}Si\equiv \rightarrow \equiv Si{-}NH{-}Si\equiv + H_2O \ \text{(water condensation)}.$$

Our calculations reported below for nitridation in silicalite do actually find this mechanism, but it turns out *not* to be the primary pathway, hence the value of the *ab initio* study. Nitridation in HY is even more complicated involving many more degrees of freedom, defying any initial intuition we may bring.

Modeling nitridation pathways in zeolites such as HY and silicalite is a daunting computational task because of the large unit cells involved, and the many degrees of freedom that likely participate during nitridation. Systems with large unit cells (>250 atoms) make periodic DFT calculations extremely slow [20]; such systems can, however, be treated with embedded-cluster methods such as ONIOM [21]. Although such cluster calculations do not include true long-range interactions present in real materials, the contributions from such interactions cancel when computing reaction barriers in sufficiently large clusters [21]. In the calculations reported below, we have used ONIOM as implemented in Gaussian codes with quantum clusters containing ~30 heavy atoms and total systems with as many as 485 heavy atoms.

The challenge then becomes finding transition states involving cooperative motions of these many degrees of freedom. The nudged elastic band (NEB) approach has emerged as the method of choice for finding elusive transition states [22]. This "chain-of-states" method has been applied to many surface science problems, especially those involving metal surfaces, and has been efficiently implemented in the VASP periodic DFT code [23]. We report below the first combined application of ONIOM and NEB, routinely using 15 system replicas in the NEB chain-of-states. Because this amounts to a total of $485 \times 3 \times 15 = 21{,}825°$ of freedom, we pay special attention below to the use of optimization algorithms that scale gently for both memory and CPU time.

We find below markedly different mechanisms for nitridation of ≡Si–O–Si≡ and ≡Si–OH–Al≡ sites, including pentavalent Si in the former case. In both cases, however, we find overall barriers on the order of 350 kJ/mol, indicating that high temperatures are generally needed for zeolite nitridation. Because these barriers are well in excess of the reaction endothermicity (~100 kJ/mol), barriers for the reverse process are also quite high, indicating that nitrided zeolites should remain relatively stable up to reasonably high temperatures.

The remainder of this article is organized as follows: in Section 2 we provide computational details of both ONIOM and NEB calculations; in Section 3 we discuss the results of reaction pathway calculations for nitridation in both HY and silicalite zeolites; and in Section 4 we offer concluding remarks.

2. Computational details

2.1. Zeolite models

All calculations in this work were performed using an assumption of a finite cluster. As shown by Fermann et al. [21], calculating energy differences between nearby configurations, such as a reaction barrier, cancels the effect of long-range slowly-varying interactions, leaving reaction energies controlled only by local electronic interactions.

We have studied silicalite and HY zeolites in this work. Silicalite (MFI-type) exhibits orthorhombic symmetry above 340 K and monoclinic symmetry below that temperature [24]. Since the substitution reaction takes place at high temperatures, the clusters have been built assuming orthorhombic symmetry [24,25]. The space group of orthorhombic silicalite is PNMA with 12 crystallographically distinct silicon atoms and 26 distinct oxygens. To investigate how nitrogen substitution reaction energies vary with oxygen location in silicalite, we computed nitridation reaction energies from clusters built around O(8) and O(13). These oxygens are representative in that O(8) has the lowest Si–O–Si angle in silicalite (155°), while O(13) has the highest (176°) [26]. Because the Si–O–Si angle is found to correlate with chemical properties such as Brønsted acid strength and ^{29}Si NMR chemical shift [1], computing nitridation energies at O(8) and O(13) will reveal the extent of variation among oxygen sites in silicalite.

Clusters with the silicalite structure were centered on either O(8) or O(13), containing 143 total silicon (tetrahedral or "T") atoms and 342 oxygen atoms, hereafter denoted 143 T clusters. Using computational methods described in detail below, we have found that nitridation energies at these sites differ by only 5 kJ/mol, less than 4% of the nitridation energy, indicating that nitridation thermodynamics is fairly insensitive to oxygen location in silicalite. It remains possible that the nitridation mechanism at O(8) may differ from that at O(13). However, because of the computationally intensive nature of these calculations, we have focused on modeling substitution at oxygen O(13) (between silicons Si(2) and Si(8)) [26], which is catalytically relevant because of its direct access to the silicalite channel intersection. Mechanistic calculations were performed on the 143 T cluster centered at O(13). All cluster models (including those of HY) were terminated with oxygen atoms fixed at their crystallographically-determined locations.

HY zeolite (FAU-type) exhibits space group $FD\bar{3}M$, with a single crystallographically distinct silicon site and four distinct oxygens [27]. Of these oxygens, O(1) and O(4) are the most accessible, being in the 12 T-ring window separating adjacent supercages. To investigate how nitrogen substitution energy var-

ies with oxygen location in HY, we computed nitridation energies from 91 T clusters built around O(1) and O(4), with a zeolite Brønsted acid strength (Si–OH–Al) at the center of each cluster. The remainder of each HY cluster is composed of silica. Oxygens O(1) and O(4) are representative by the following argument. Of the accessible locations O(1), O(2) and O(4) (O(3) is buried in the double 6-ring), O(1) and O(4) have the lowest and highest proton siting energies, separated by 15–20 kJ/mol [21]. We have found that nitridation energies at these sites differ by only 3 kJ/mol, indicating that nitridation thermodynamics is relatively insensitive to location in HY, as it is in silicalite. We thus focused on computing nitridation mechanisms in HY with a 91 T cluster centered at O(1).

2.2. Computational details

The embedded-cluster approach via 2-layer ONIOM [28–31] was used for obtaining optimized geometries and energies in the present study. The quantum layer of the silicalite cluster centered on O(13) contained 11 T sites, and the outer layer contained 132 T sites, for a total of 143 T sites in the total system (denoted "S"). (The silicalite cluster centered on O(8) was 8T quantum/143 T total system.) For the HY cluster centered on O(1), the sizes are 10 T quantum cluster plus 81 T outer layer giving a total system size of 91 T. (The HY cluster centered on O(4) was 12 T quantum/84 T total system.) We have previously shown that such cluster sizes converge reaction energies of acid–base reactions in zeolites with respect to system size [21]. These particular sizes depend on the crystal structures of the two materials, and are based on building chemically reasonable cluster models (no dangling rings) that are sufficiently large to capture local electronic interactions, but small enough to be tractable for all-electron calculations.

No electrostatic interaction between the inner and outer layer was considered, i.e., the calculations were performed using "mechanical embedding" but not "electronic embedding." The inner layers were terminated at oxygen atoms, with dangling bonds saturated by adding hydrogen atoms placed along O–Si vectors to form the quantum clusters (denoted "C"). In general, we apply ONIOM to zeolites by allowing all atoms to move except for the atoms that terminate the total system. However, for silicalite, this procedure was found to cause unacceptable distortions of the quantum cluster geometry because of mechanical instability of the cluster representation. We solved this problem by keeping the outer-layer atoms fixed at their crystallographic positions, hence providing a rigid mechanical embedding. The silicalite quantum cluster was made large enough to keep the rigid constraints sufficiently far from the nitridation site. This mechanical instability did not arise in our studies of HY.

The total system electronic energy is approximated within ONIOM from three different calculations according to [32]:

$$E_{\mathrm{ONIOM}} = E_{\mathrm{hi}}(\mathrm{C}) + E_{\mathrm{lo}}(\mathrm{S}) - E_{\mathrm{lo}}(\mathrm{C}), \quad (1)$$

where the subscripts "hi" and "lo" represents high and low levels of theory, respectively. For the high level of theory, we used B3LYP/6-311G(d,p) [33–35], which we have found reproduces zeolite geometries and vibrational frequencies (with appropriate scaling factors [36]), and captures ~90% of the barrier for proton transfer in HY [37] . We found that capturing the remaining 10% of the barrier requires MP2/MP4 calculations [37], which are beyond the scope of our computational resources for the quantum clusters considered herein.

For the low level of theory, we applied the "universal force field" (UFF) [38] with oxygen and nitrogen atom types specified as O_3_z and N_3, respectively. We chose UFF as the low level of theory because of its broad applicability, avoiding the need to reparameterize for new elements such as nitrogen. UFF also has a zeolite-specific oxygen (O_3_z). Although UFF is not a reactive force field, we have shown in previous work that accurate reaction energies can nonetheless be obtained [21]. The downside of using UFF within ONIOM, as stated above, is that its inaccuracies cause distortions to the silicalite structure, which we have dealt with by keeping outer-layer atoms fixed. The QM-Pot method of Sauer and Sierka [39] would address this through its use of carefully optimized forcefields, requiring reparameterization for novel compositions. For HY, which has a flexible outer layer, geometry optimizations were performed using the "quadratic coupling" method of Vreven et al. [40,41], which couples forces between the layers in a numerically stable fashion. In general, the clusters were optimized without any symmetry constraint.

Transition state calculations were performed using the Berny optimization algorithm [42]. The intial configuration of a transition state search was either guessed or generated by using the nudged elastic band (NEB) method [22]. We were reasonably successful at guessing for silicalite; however, for HY the NEB method was crucial for finding transition states. The implementation of NEB along with ONIOM is discussed in Appendix A. In general, we have followed the following strategy for finding transition states:

- Geometry optimizations were performed to find local potential minima (reactants, products and intermediates) using ONIOM: B3LYP/6-311G(d,p)//UFF. All minima were confirmed with frequency analysis.
- Using all combinations of the potential minima, initial reaction pathways were generated using linear interpolation including 15 images between the two endpoints.
- The NEB forces were then calculated using an external script, with "true" forces obtained by ONIOM calculations as described above. Because of computational expense, these NEB calculations were performed using the BLYP pure functional [33,34] and the 6-31g(d) basis set [43,44] for the quantum cluster. The tangent was obtained using the Improved Tangent NEB approach [45], and the saddle point obtained by the Climbing Image NEB method [46].
- The NEB elastic band was optimized until the NEB forces are less than 0.1 eV/Å.
- The highest energy image in a given NEB chain was then taken as the initial guess for a transition state search using Berny optimization (using B3LYP/6-311g(d,p)).

The validity of each transition state was confirmed by computing normal modes at the saddle point, then performing geometry optimizations along both directions of the reaction coordinate to confirm that these optimizations relax to the desired local minima. For silicalite clusters, we generally obtain several imaginary frequencies because of the constrained outer layer.

In these cases, we recalculated normal modes using artificially high masses for constrained atoms (10^4 amu), which shrink the moduli of the spurious imaginary frequencies, helping to identify the physically correct reaction coordinate. This helped to eliminate many but not all spurious imaginary frequencies. The correct reaction coordinates that lead to the desired reactants and products were then identified by inspection of the remaining relevant normal modes. All calculations were performed using Gaussian Development Version (Release D.02) [47] on Linux workstations.

Reaction paths are labelled below with bare electronic energies. As such, all energy differences (ΔV) shown below are between electronic energies at critical points on the nitridation potential surface. To explore entropic effects, we will report in a forthcoming publication the solution of a microkinetic model inspired by these DFT calculations, using rate constants computed from harmonic transition state theory.

3. Results and discussion

Here we discuss the results of our nitridation pathway calculations for silicalite and HY. All nitridation pathways begin with adsorbed ammonia. Snapshots of adsorbed NH_3 in silicalite and HY are shown in Figs. 1 and 2, respectively. Also, snapshots of the nitridation products—adsorbed water in nitrogen-substituted silicalite and HY—are shown in Figs. 3 and 4, respectively. We discuss below the adsorption energies of these species in the context of their respective nitridation pathways. Movies and still images of the complete reaction pathways can be found online in Supplementary material.

3.1. Reaction pathway of nitridation in silicalite

The nitridation mechanism in silicalite was computed without the aid of NEB. Instead, we studied the two-step mechanism discussed in the Introduction: ammonolysis followed by water condensation. In the first step, adsorbed ammonia (AA) attacks the framework from the channel to form an intermediate, which reacts further to give the nitrided zeolite and adsorbed water (AW) in the pentasil cage.

We begin by discussing our results for the adsorption and reaction energies in silicalite. We note that there are two different reaction energies, and each deserves mention. The first reaction energy (ΔV_{rxn}(ads)) is from adsorbed ammonia in untreated zeolite to adsorbed water in nitrided zeolite; this is important for computing reaction pathways which begin with ammonia–zeolite complexes, and end with water–zeolite products. The second reaction energy (ΔV_{rxn}(gas)) is from gas-phase ammonia and untreated zeolite to gas-phase water and nitrided zeolite; this is important for establishing overall nitridation yields when constraining gas-phase ammonia and water concentrations in kinetic equation. The two reaction energies are related by:

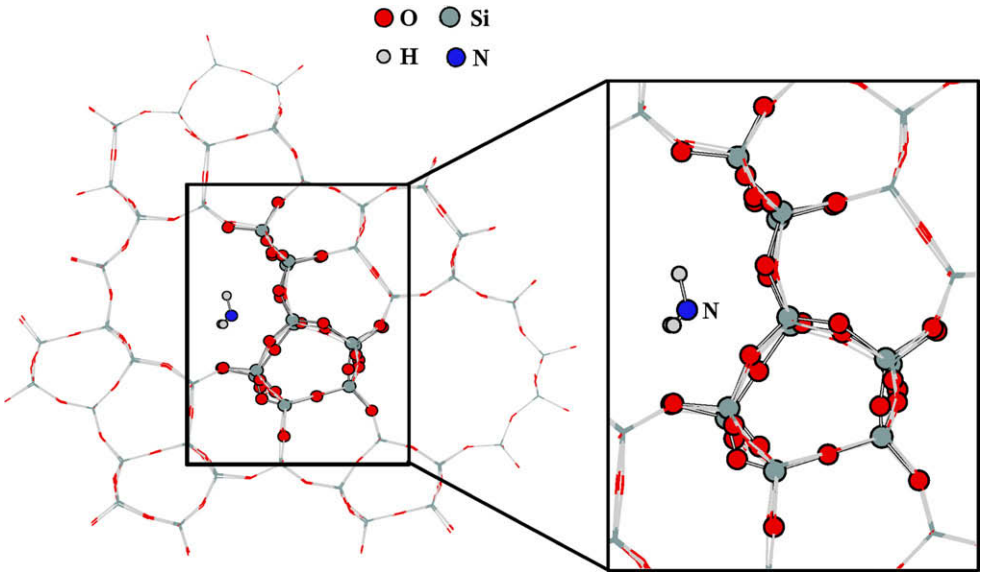

Fig. 1. Snapshot of adsorbed ammonia (AA) inside 11 T cluster embedded in 143 T total system of silicalite zeolite.

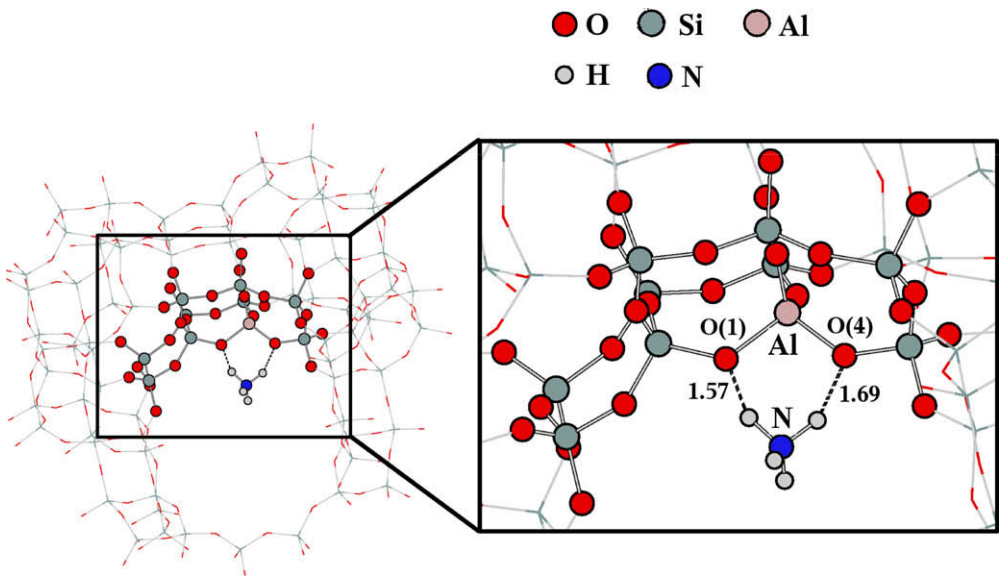

Fig. 2. Snapshot of strongly adsorbed (SA) ammonia inside 10 T cluster embedded in 91 T total system of HY zeolite.

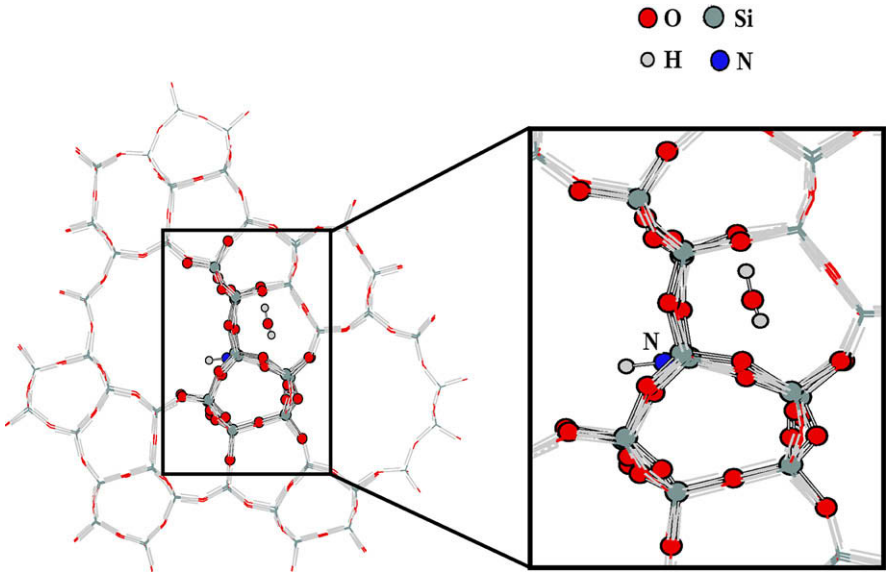

Fig. 3. Snapshot of adsorbed water (AW) inside 11 T cluster embedded in 143 T total system of nitrogen substituted silicalite zeolite.

$$\Delta V_{rxn}(\text{gas}) = \Delta V_{rxn}(\text{ads}) + \Delta V_{ads}(\text{amm/zeo}) - \Delta V_{ads}(\text{wat/Nzeo}), \quad (2)$$

where ΔV_{ads}(amm/zeo) is the (negative) adsorption energy of ammonia in the untreated zeolite, and ΔV_{ads}(wat/Nzeo) is the (negative) adsorption energy of water in the nitrided zeolite.

Using the DFT/ONIOM methods as described above, the computed reaction and adsorption energies at O(13) in silicalite are ΔV_{rxn}(ads) = 158 kJ/mol, ΔV_{ads}(amm/zeo) = −41 kJ/mol and ΔV_{ads}(wat/Nzeo) = −15 kJ/mol, giving ΔV_{rxn}(gas) = 132 kJ/mol. Repeating these energy calculations at O(8) in silicalite gives virtually identical adsorption energies, and the nitridation energy ΔV_{rxn}(ads) = 153 kJ/mol, indicating very little dependence on siting inside the silicalite lattice.

The computed desorption energy for ammonia in silicalite at O(13) is 41 kJ/mol, while experiments report 57–65 kJ/mol [48]. The computed desorption energy for water in the pentasil cage of the nitrided zeolite is 15 kJ/mol, while experiments on water in silicalite give 25–32 kJ/mol [49,50]. These discrepancies arise from the following, in order of likely decreasing importance: (i) the use of the B3LYP functional which does not capture van der Waals forces, (ii) the finite cluster approximation, (iii) the fact that no experimental data exists for water adsorbed in nitrided zeolites, and (iv) the fact that we computed local minima and did not thermally average over the silicalite adsorption-energy landscape. We are nonetheless encouraged that our calculations capture the fact that ammonia is more strongly adsorbed in silicalite than is water. As discussed above, these approximations are most severe for adsorption energy calculations; our computed intermediate energies and barriers are essentially converged with respect to system size [21], and are much less sensitive to contributions from van der Waals forces.

We then performed geometry optimizations to search for plausible reaction intermediates, finding four different likely intermediates. The structures of two of these intermediates are shown in Fig. 5. In the intermediates shown in Fig. 5, the –NH_2 group points

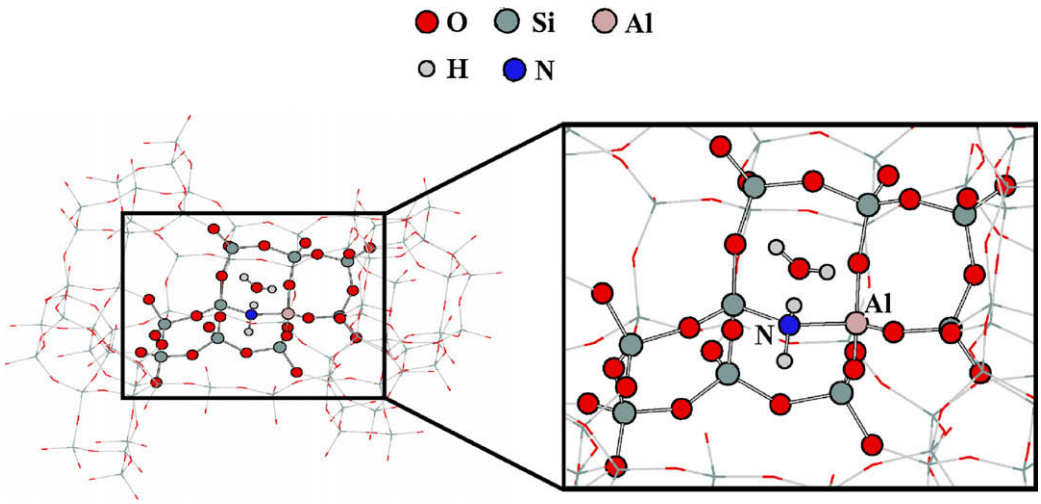

Fig. 4. Snapshot of adsorbed water (AW2) inside 10 T cluster embedded in 91 T total system of nitrogen substituted HY zeolite.

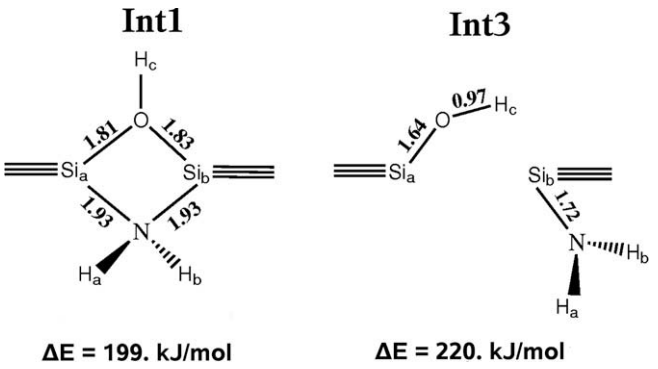

Fig. 5. Possible reaction intermediates inside silicalite and energy comparison to adsorbed NH_3 (AA).

towards the straight channel while the –OH group points towards the pentasil cage. The other two intermediates are mirror images of the ones shown in Fig. 5.

In Int1, a planar four-atom ring is formed with connectivity $\equiv Si<^{N}_{O}>Si\equiv$, involving pentavalent Si atoms. The coordination structure around Si is nearly trigonal bipyramidal indicating sp^3d hybridization, with nitrogen in an axial position. The computed Si–N bond length (1.9 Å) is higher than the usual Si–N bond length (1.75 Å). Similarly, the 4-ring oxygen has an Si–O bond length of about 1.8 Å, which is longer than typical Si–O bonds (1.6 Å). This finding is qualitatively consistent with Gutmann's rule, which states that short intermolecular (Si–N) bonds cause lengthening of intramolecular (Si–O) bonds [51]. The bonding around pentavalent Si in this system can be understood by recalling that, besides forming σ bonds, the vacant d-orbitals of silicon can form $p_\pi - d_\pi$ bonds with π systems or with atoms containing unshared p electrons (halogens, oxygen, nitrogen, etc.), yielding five- and six-coordinated silicon complexes [52,53].

In Int3, the zeolite framework becomes interrupted by ammonolysis yielding $\equiv Si–OH + H_2N–Si\equiv$ groups. The energies of Int1 and Int3 relative to adsorbed ammonia—199 and 220 kJ/mol, respectively—indicate that while both are high in energy, the 4-ring in Int1 is significantly favored over the interrupted framework in Int3, a surprising result. We have carried out transition state searches using Int1 as the intermediate structure. Important geometrical parameters for Int1 are listed in Table 1 using the numbering scheme shown in Fig. 6.

The transition state for the first step (TS1) connecting AA to Int1 is shown in Fig. 7. The energy of TS1 relative to AA is 314 kJ/mol; important geometrical parameters are listed in Table 1. In TS1, nitrogen forms a bond with Si_a as indicated by the N–Si_a distance decreasing from 3.22 Å in AA to 1.78 Å in TS1. At the same time, the Si_a–O bond weakens as indicated by the Si_a–O bond lengthening from 1.62 Å to 1.96 Å. Also, an ammonia hydrogen, H_c, breaks away from nitrogen to form a bond with oxygen.

Moving through TS1 towards Int1 involves completing the transfer of H_c from nitrogen to oxygen, while forming a new N–Si_b bond to complete the 4-ring $\equiv Si<^{N}_{O}>Si\equiv$. To complete the nitridation, an additional hydrogen (H_a) must be transferred from nitrogen to oxygen, while breaking the two Si–O bonds. This is partially accomplished in TS2 shown in Fig. 7 (E_{TS2} = 343 kJ/mol), in which the Si_b–O bond has broken, replaced by a nascent O–H_a bond. The N–Si_b bond length in TS2 is 1.75 Å, characteristic of a fully formed N–Si bond.

In the product configuration, water is adsorbed in a nitrided pentasil cage. The Si–N bond lengths are ~1.7 Å and Si–N–Si bond angle is 140°, values that match the Si–N bond length (1.68–1.70 Å) and Si–N–Si angle (135–138°) obtained from our periodic DFT calculations on nitrided sodalite [16]. The full silicalite nitridation energy diagram is shown in Fig. 8. The predicted barrier for the first step is 314 kJ/mol while that for the second step is 143 kJ/mol, with an overall barrier of 343 kJ/mol. Beyond the numbers, the hallmark of this two-step process is the formation of a 4-ring $\equiv Si<^{N}_{O}>Si\equiv$ intermediate with pentavalent Si.

Table 1
Important geometrical parameter of various steps of nitridation in silicalite (distances in Å, angles in °).

Adsorbed NH_3 (AA)			
Si_a–N	3.22	N–H_a(H_b or H_c)	1.02
Si_b–N	3.31	O–H_a	3.68
O–N	3.22	O–H_b	3.78
Si_a–O	1.62	O–H_c	3.63
Si_b–O	1.62	Si_a–O–Si_b	154
TS1			
Si_a–N	1.78	O–H_c	0.98
Si_b–N	3.39	N–H_a(H_b)	1.01
O–N	2.5	N–H_c	2.24
Si_a–O	1.96	Si_a–O–Si_b	128
Si_b–O	1.70	N–H_c–O	93
O–H_a	2.89	Si_b–O–H_c	105
O–H_b	3.34		
4-ring Intermediate (Int1)			
Si_a–N	1.93	N–H_a(H_b)	1.02
Si_b–N	1.93	Si_a–N–Si_b	101
Si_a–O	1.81	Si_a–O–Si_b	110
Si_b–O	1.83	H_a–N–H_b	107
O–H_a	2.69	Si_a–O–H_c	124
O–H_b	3.12	Si_b–O–H_c	124
O–H_c	0.96	N–Si_a–O	73
N–O	2.22	N–Si_b–O	72
TS2			
Si_a–N	1.84	N–H_a	1.2
Si_b–N	1.75	N–H_b	1.02
Si_a–O	2.11	Si_a–N–Si_b	132
Si_b–O	3.06	Si_a–O–Si_b	77
O–H_a	1.32	H_a–N–H_b	121
O–H_b	3.14	Si_a–O–H_c	115
O–H_c	0.96	N–H_a–O	130
N–O	2.29	N–Si_a–O	73
Adsorbed Water (AW)			
Si_a–N	1.71	N–O	2.96
Si_b–N	1.7	N–H_b	1.02
Si_a–O	2.76	Si_a–N–Si_b	140
Si_b–O	3.02	Si_a(Si_b)–N–H_b	110
O–H_a(H_c)	0.97	H_a–O–H_c	104
O–H_b	3.86		

3.2. Reaction pathway of nitridation in HY

To determine nitridation pathways in HY, we used NEB which requires specification of pathway endpoints, i.e., structures of reactant and product. The reactant for nitridation in HY is a strongly adsorbed (SA) ammonia species that results from the acid–base reaction of ammonia with the zeolite Brønsted acid site ≡Si–OH–Al≡. The structure of SA, shown in Fig. 2, is NH_4^+ in a bidentate complex with O(1) and O(4) (O(1)–H_a = 1.57 Å, O(4)–H_d = 1.69 Å). The presumed product of HY nitridation at O(1) is adsorbed water (AW2) in the HY hexagonal prism, interacting with the newly formed $\equiv Si–NH_2–Al\equiv$ group at the O(1) site.

The computed reaction and adsorption energies at O(1) in HY are ΔV_{rxn}(ads) = 98 kJ/mol, ΔV_{ads}(amm/zeo) = −111 kJ/mol and ΔV_{ads}(wat/Nzeo) = −42 kJ/mol, giving ΔV_{rxn}(gas) = 29 kJ/mol. We note that while still endothermic, the value of ΔV_{rxn}(gas) for HY nitridation is quite a bit lower than that in silicalite, suggesting the possibility of higher nitridation yields in HY.

Repeating the nitridation energy calculation at O(4) in HY gives ΔV_{rxn}(ads) = 95 kJ/mol, once again indicating very little dependence on siting inside the zeolite. (The adsorption energies are

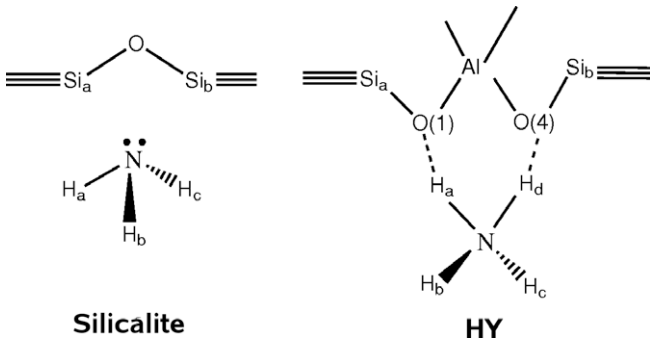

Fig. 6. Numbering scheme for ammonia in silicalite and HY.

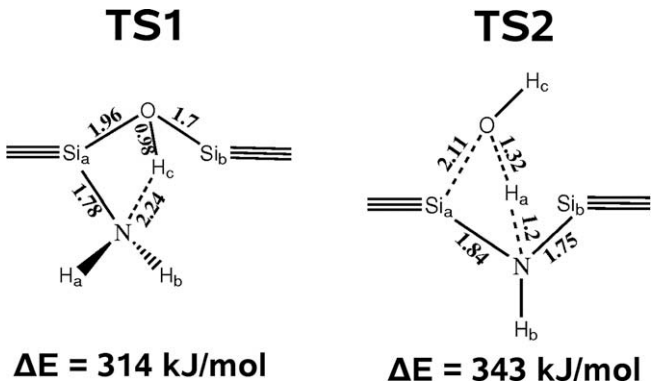

Fig. 7. Structures of transition states connecting adsorbed ammonia (AA) to nitrided silicalite with adsorbed water (AW).

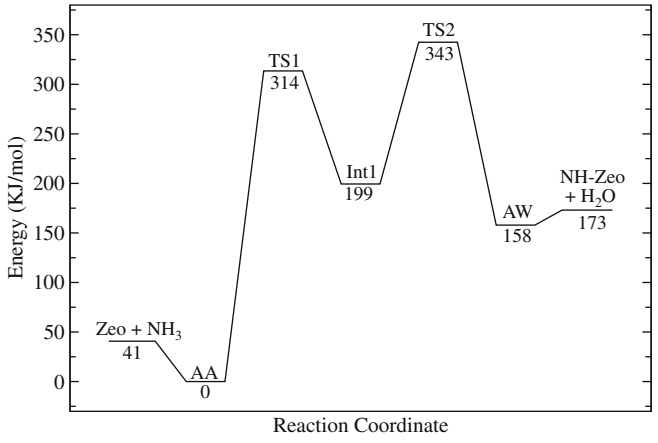

Fig. 8. Energy profile for reaction pathway of nitridation of silicalite.

identical because of the bidentate nature of ammonia–HY complexation.) Because protonation at O(1) is more favorable than that at O(4) by 15–20 kJ/mol [21], we focus below on computing nitridation pathways at O(1) in HY.

Our computed desorption energy for ammonia in HY is 111 kJ/mol, which agrees broadly with experimental values in the range 100–130 kJ/mol [54–56]. The shorter O(1)–H$_a$ bond follows from the fact that O(4) is more acidic than is O(1) [57]. These results are in excellent agreement with previous calculations on ammonia adsorption in acidic zeolites [58–61], which generally find ammonium ion in bidentate or even tridentate coordination with the anionic framework. We note that these previous calculations involved embedded quantum clusters as small as 3 T, while we are using 10 T quantum clusters, indicating that the structure and energy of SA is reasonably well-converged with respect to system size. Our predicted desorption energy for AW2 is 42 kJ/mol, indicating that water is more strongly bound in the hexagonal prism of nitrided HY than in the pentasil cage of nitrided silicalite.

We identified two pathways for nitridation of HY. The first pathway is a simple two-step mechanism whereas the second pathway is a much more complicated 5-step process. The energy profiles for the two pathways are shown in Figs. 9 and 10. The overall barrier for pathway I is 359 kJ/mol while that for pathway II is 400. kJ/mol. The relative simplicity and lower overall barrier of pathway I suggest that it is the more likely mechanism of the two. We have thus used pathway I for further studies. We do not provide further discussion of pathway II; more information about the intermediates and transition states of pathway II can be found in Supplementary material.

The energy profile for HY nitridation is shown in Fig. 9, and important geometrical parameters are given in Table 2. The H$_d$ atom leaves O(4) (H$_d$–O(4) increases from 1.69 Å in SA to 3.64 Å in TS1) and H$_a$ leaves nitrogen to form TS1. Nitrogen starts to form a weak bond with Si$_a$ (Si$_a$–N = 2.49 Å). The Si$_a$–N bond further strengthens in Int1 (Si$_a$–N = 2.17 Å). The structures of Int1 and TS1 are quite similar with a slightly stronger Si$_a$–N bond in Int1. This is also clear from the difference in energies of Int1 and TS1, which is only 2.2 kJ/mol. The energy barrier for the first step is predicted to be 118 kJ/mol, comparable to the desorption energy of

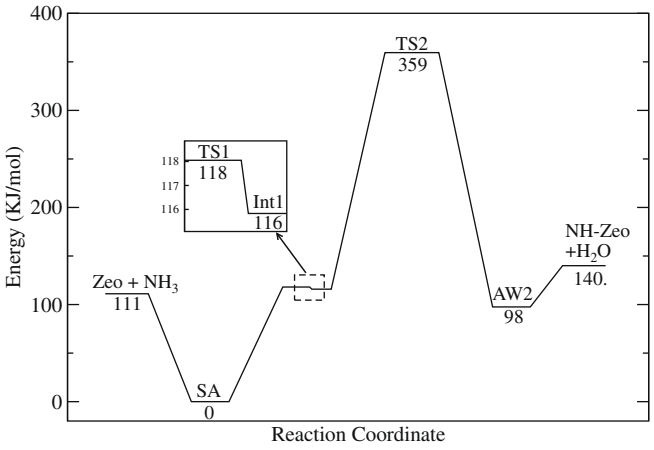

Fig. 9. Energy profile for reaction pathway I of HY nitridation.

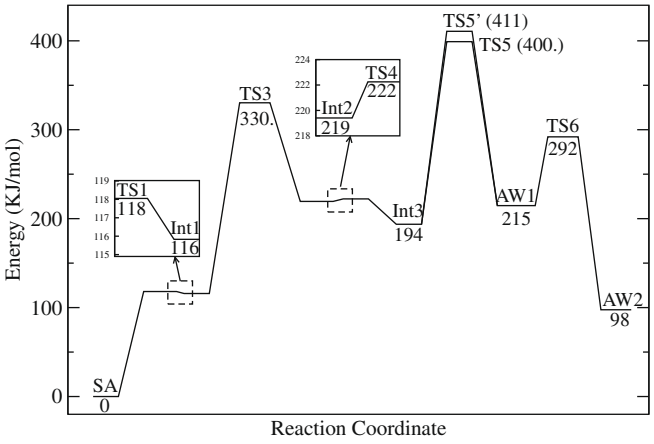

Fig. 10. Energy profile for reaction pathway II of HY nitridation.

Table 2
Important geometrical parameters of various steps of nitridation in HY (distances in Å, angles in °).

Strongly Adsorbed NH_3 (SA)			
Si_a–O(1)	1.64	N–H_d	1.06
Al–O(1)	1.83	N–H_b(H_c)	1.02
Al–O(4)	1.81	N–Al	3.34
Si_b–O(4)	1.63	Si_a–O(1)–Al	129
O(1)–H_a	1.57	Al–O(4)–Si_b	137
O(4)–H_d	1.69	O(1)–Al–O(4)	103
N–H_a	1.08	H_a–N–H_d	100
TS1			
Si_a–O(1)	1.75	N–H_b(H_c or H_d)	1.02
Al–O(1)	1.94	N–Si_a	2.49
Al–O(4)	1.73	Si_a–O(1)–Al	132
Si_b–O(4)	1.61	Al–O(4)–Si_b	138
O(1)–H_a	0.97	Si_a–O(1)–H_a	109
O(4)–H_d	3.64	Al–O(1)–H_a	101
N–H_a	3.41		
Int1			
Si_a–O(1)	1.77	N–H_b(H_c or H_d)	1.02
Al–O(1)	1.93	N–Si_a	2.17
Al–O(4)	1.73	Si_a–O(1)–Al	131
Si_b–O(4)	1.61	Al–O(4)–Si_b	136
O(1)–H_a	0.97	Si_a–O(1)–H_a	109
O(1)–H_d	2.75	Al–O(1)–H_a	99
N–H_a	3.38		
TS2			
Si_a–O(1)	2.82	N–H_b(H_c)	1.02
Al–O(1)	1.85	Si_a–H_d	2.14
Al–N	3.23	Al–H_d	2.24
Si_a–N	1.78	Al–O(1)–H_a	112
O(1)–H_a	0.97	Si_a–H_d–Al	170
O(1)–H_d	1.16	Al–O(1)–H_d	93
N–H_a	2.96	Si_a–N–H_d	88
N–H_d	1.27	N–H_d–O(1)	169
Adsorbed Water (AW2)			
Si_a–O(1)	3.7	N–H_b(H_c)	1.01
Al–O(1)	3.71	H_a–O(1)–H_d	105
Al–N	2.11	Al–N–Si_a	122
Si_a–N	1.81	H_b–N–H_c	105
O(1)–H_a(H_d)	0.96		

ammonia in HY (SA structure). As such, the first step of HY nitridation is activation of ammonia to form a more free and reactive form of ammonia.

The transition state for the second step (TS2) is shown in Fig. 11. In TS2, nitrogen forms a bond with Si_a (Si_a–N = 1.78 Å) while the O(1)–Si_a bond breaks (Si_a–O(1) = 2.82 Å). The H_d atom starts leaving nitrogen (N–H_d = 1.27 Å) and starts to form a bond with O(1) (O(1)–H_d = 1.6 Å). H_d lies collinear and midway between Si_a and Al (Si_a–H_d–Al = 170°), also collinear between nitrogen and O(1) (N–H_d–O(1) = 169°).

In the final product (AW2), water forms a physisorbed state inside the hexagonal prism (double 6-Ring) of HY. The energy barrier for the second step is 244 kJ/mol. Nitrogen forms a bond with four atoms; as such the Si_a–N (1.81 Å) and Al–N (2.11 Å) bond lengths are larger than usual. The energy barrier for the opposite step, i.e., AW2 to Int1 is 262 kJ/mol, indicating that the nitrided HY is kinetically relatively stable.

3.3. Summary and comparison of mechanisms

Nitridation of both HY and silicalite is predicted to be two-step processes, wherein adsorbed NH_3 reacts with the zeolite frame to form an intermediate that reacts further to give the nitrided zeolite and adsorbed water. The overall barrier for nitridation of silicalite is 343 kJ/mol while that for HY is 359 kJ/mol, suggesting why high temperatures are required in nitridation experiments. The key intermediate predicted for the process in silicalite is a surprising "4-ring" structure with pentavalent silicon. The key intermediate in pathway I of HY nitridation (Int1) does *not* exhibit this 4-ring structure. In the more complex and higher-energy pathway II of HY nitridation, a similar 4-ring intermediate (denoted as Int2 in Fig. 10) has been discovered by our NEB/ONIOM calculations. This 4-ring lies higher in energy than the 4-ring in silicalite. This may be because O(1) in HY lies in the hexagonal prism, which is more constrained than the pentasil cage of silicalite. The 4-ring intermediate may be preferred for nitridation of HY at O(4) or O(2), since these oxygens lie towards the more spacious sodalite cage. These issues will be explored in a forthcoming publication.

Also a surprise is the prediction in HY pathway I that the Si–O bond breaks before the Al–O bond. For the Al– bond to break and a new Al–N bond to form, the ammonia would have to approach the framework aluminum. However, when that happens, the bidentate NH_4^+ complex spontaneously forms, bringing the system back to its reactant state (denoted SA). As such, pathway I for HY nitridation involves breaking the Si–O bond first, keeping ammonia sufficiently far from aluminum.

4. Concluding remarks

We have performed embedded-cluster calculations using density functional theory to investigate mechanisms of nitrogen substitution (nitridation) in HY and silicalite zeolites. We consider nitridation as replacing Si–O–Si and Si–OH–Al linkages with Si–NH–Si and Si–NH_2–Al, respectively. From gas-phase ammonia and untreated zeolite, to gas-phase water and nitrided zeolite,

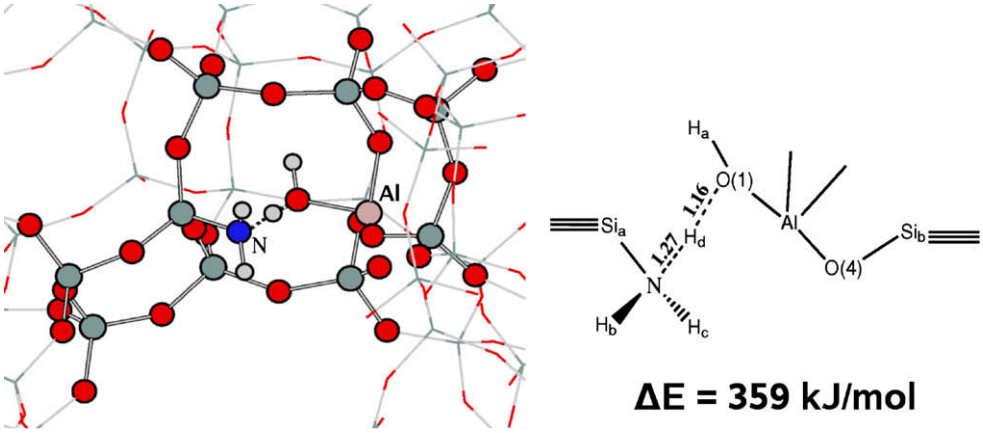

Fig. 11. Transiton state converting Int1 to AW2 for reaction pathway I.

we predict that nitridation is much less endothermic in HY (29 kJ/mol) than in silicalite (132 kJ/mol), indicating the possibility of higher nitridation yields in HY.

To reveal mechanistic details, we have combined for the first time the nudged elastic band (NEB) method of finding elusive transition states, with the ONIOM method of treating embedded quantum clusters. We have considered quantum clusters with ~30 heavy atoms, total system sizes with as many as 485 atoms, and total degrees of freedom as many as 21,825 in NEB calculations. We predict that nitridation of silicalite proceeds via a planar intermediate involving a $\equiv Si<^{N}_{O}>Si\equiv$ ring with pentavalent Si, whereas nitridation of HY is found to proceed via an intermediate similar to physisorbed ammonia. We also discovered an unlikely 5-step mechanism for HY nitridation, which has a higher barrier than that for the two-step pathway. B3LYP/6-311G(d,p) calculations give an overall barrier for silicalite nitridation of 343 kJ/mol, while that in HY is 359 kJ/mol. Although the overall nitridation barriers are relatively high, requiring high temperatures for substitution, the overall barriers for the reverse processes are also high. As such, we predict that once these catalysts are made, they remain relatively stable.

For nitrided zeolites to be useful catalysts, their stabilities to heat and humidity must be investigated and understood. In a forthcoming publication, we will apply these mechanisms to develop rate equations describing nitridation yields. We will also study the reverse processes to investigate the stability of these nitrided materials to heat and humidity.

Acknowledgments

We thank K. Hammond, Dr. G. Tompsett and Dr. J. T. Fermann at UMass Amherst; Dr. T. Vreven at UMass Worcester; and Dr. D. Fox at Gaussian, Inc. for their expertise. We also thank Prof. C. Grey and F. Dogan at Stony Brook University for stimulating discussions and collaborations on nitrided zeolites. We are grateful for generous funding from the National Science Foundation (CBET-0553577) and the Department of Energy (DEFG027ER15918).

Appendix A. Implementation of NEB with ONIOM

NEB is a method for mapping out the minimum energy path (MEP) between a pair of stable minima on a potential energy surface, without any prior knowledge of the location of the transition state or the nature of the reaction coordinate [22]. NEB is a chain-of-states method in which adjacent system replicas are joined together with springs to represent the reaction pathway. Minimizing the NEB force (see below) converges the chain to the MEP. At each step in the optimization, the chain represents the present best guess to the MEP. The NEB force is the sum of the component of the true force locally perpendicular to the chain, and the component of the spring force parallel to the chain. The NEB force on the ith image is thus given by:

$$\vec{F}_i = \vec{F}^{s}_{i\parallel} + \vec{F}^{t}_{i\perp}. \tag{A.1}$$

The parallel component of the spring force prevents the images from running downhill away from the transition state, while the perpendicular component of the true force pulls the images towards the MEP. The parallel component of the spring force is estimated as:

$$\vec{F}^{s}_{i\parallel} = \left(k[(\vec{P}_{i+1} - \vec{P}_i) - (\vec{P}_i - \vec{P}_{i-1})] \cdot \hat{\tau}_i\right)\hat{\tau}_i, \tag{A.2}$$

while the perpendicular component of the true force is computed as:

$$\vec{F}^{t}_{i\perp} = -\nabla V(\vec{P}_i) - \left(-\nabla V(\vec{P}_i) \cdot \hat{\tau}_i\right)\hat{\tau}_i. \tag{A.3}$$

In the above expressions, $\vec{P}_i$ is the $3N_{atoms}$-dimensional position vector of the ith image, k is the spring constant, and $\hat{\tau}_i$ is the unit tangent vector on the ith image.

The simplest estimate of the ith unit tangent vector is obtained from the normalized line segment joining the adjacent images according to:

$$\hat{\tau}_i = \frac{\vec{P}_{i+1} - \vec{P}_{i-1}}{\left|\vec{P}_{i+1} - \vec{P}_{i-1}\right|}. \tag{A.4}$$

Using this approximate tangent, it has been found that kinks in the path may develop when the force parallel to the MEP is large compared to the force perpendicular to the MEP, and when many images are used [45]. To overcome this difficulty, an "improved tangent" (IT-NEB) method has been developed [45], which we use in our calculations below. To converge to the saddle point, "climbing image" NEB (CI-NEB) is used below; in this approach the springs to the highest-energy image are released, and this image is made to climb in the direction opposite to the parallel component of the true force, leading the image to the saddle point [46].

We have implemented a parallel NEB object-oriented program interfacing with G03 and GDV [47] (used for force and energy calculation via ONIOM calculation). To the best of our knowledge, this is the first implementation of NEB with ONIOM (using the Gaussian quantum chemistry package). Although there is a previous implementation of NEB with G98 by Alfonso and Jordan [62], this does not include interfacing with ONIOM. Since the systems we are treating involve many degrees of freedom—in particular, $N_{total} = 3 \times N_{atoms} \times N_{images}$ as high as 21,825—we we have implemented optimizers that scale gently with system size for memory and CPU time, including the Newton damped dynamics (NDD) method [62,63], and the modified Broyden method (Srivastava's formulation for large systems) [64].

The most expensive step in this algorithm is the energy/force calculation using ONIOM (e.g., ~42 min per ONIOM energy/force calculation for HY on two Xeon 3.00 GHz processors). The NEB force/energy calculation constitutes an "embarrassingly" parallel problem because of the independence of the replicas, meaning we should expect to obtain nearly linear speed-ups by using multiple processors. Indeed, in the calculations reported below, when using five processors the calculations speed up by approximately a factor of 5.0.

Appendix B. Supplementary material

Supplementary data associated with this article can be found, in the online version, at doi:10.1016/j.jcat.2009.10.015.

References

[1] S.M. Auerbach, K.A. Carrado, P.K. Dutta, Handbook of Zeolite Science and Technology, Marcel Dekker Inc., New York, 2003.
[2] G.W. Huber, S. Iborra, A. Corma, Synthesis of transportation fuels from biomass: chemistry, catalysts, and engineering, Chemical Reviews 106 (9) (2006) 4044–4098.
[3] K.D. Hammond, S.M. Auerbach, Modeling the structure and spectroscopy of alkaline zeolites, in: Silica and Silicates in Modern Catalysis, in press.
[4] K.D. Hammond, F. Dogan, G.A. Tompsett, V. Agarwal, J.W. Curtis Conner, C.P. Grey, S.M. Auerbach, Spectroscopic signatures of nitrogen substituted zeolites, Journal of American Chemical Society 130 (45) (2008) 14912–14913.
[5] G.T. Kerr, G.F. Shipman, Reaction of hydrogen Zeolite Y with ammonia at elevated temperatures, Journal of Physical Chemistry 72 (8) (1968) 3071.
[6] P. Fink, J. Datka, Infrared spectroscopic studies of amination of ZSM-5 zeolites, Journal of the Chemical Society-Faraday Transactions I 85 (Part 10) (1989) 3079–3086.
[7] S. Ernst, M. Hartmann, S. Sauerbeck, T. Bongers, A novel family of solid basic catalysts obtained by nitridation of crystalline microporous aluminosilicates and aluminophosphates, Applied Catalysis A – General 200 (1–2) (2000) 117–123.
[8] S. Ernst, M. Hartmann, T. Hecht, P.C. Jaen, S. Sauerbeck, The influence of water on the activity of nitridated zeolites in base-catalyzed reactions, in: R. Aiello, G.

Giordano, F. Testa (Eds.), Impact of Zeolites and Other Porous Materials on the New Technologies at the Beginning of the New Millennium, Pts A and B, vol. 142 of Studies In Surface Science And Catalysis, 2002, 2nd International Conference of the Federation-Of-European-Zeolite-Associations, Taormina, Italy, September 01–05, 2002, pp. 549–556.
[9] K. Narasimharao, M. Hartmann, H.H. Thiel, S. Ernst, Novel solid basic catalysts by nitridation of zeolite beta at low temperature, Microporous and Mesoporous Materials 90 (1–3) (2006) 377–383.
[10] M. Srasra, G. Poncelet, P. Grange, S. Delsarte, Nitrided ultrastable zeolite Y: identification and quantification of incorporated nitrogen species and their influence on the basic catalytic activity, in: J. Cejka, N. Zilkova, P. Nachtigall (Eds.), Molecular Sieves: From Basic Research to Industrial Applications, Pts. A And B, vol. 158 of Studies in Surface Science and Catalysis, 2005, 3rd Conference of the Federation-of-European-Zeolite-Association, Prague, Czech Republic, August 23–29, 2005, pp. 1811–1818.
[11] A.J. Han, Y. Zeng, J. Guo, Y.F. Huang, H.Y. He, Y.C. Long, Interaction of methylamine with highly siliceous MFI, FAU and FAU and FER-type zeolites, Chinese Journal Of Chemistry 23 (4) (2005) 413–417.
[12] A.J. Han, H.Y. He, J. Guo, H. Yu, Y.F. Huang, Y.C. Long, Studies on structure and acid–base properties of high silica MFI-type zeolite modified with methylamine, Microporous and Mesoporous Materials 79 (1–3) (2005) 177–184.
[13] A.J. Han, J. Guo, H. Yu, Y. Zeng, Y.F. Huang, H.Y. He, Y.C. Long, The leading role of association in framework modification of highly siliceous zeolites with adsorbed methylamine, Chem. Phys. Chem. 7 (3) (2006) 607–613.
[14] J. Guo, A.-J. Han, H. Yu, J.-P. Dong, H. He, Y.-C. Long, Base property of high silica MFI zeolites modified with various alkyl amines, Microporous and Mesoporous Materials 94 (1–3) (2006) 166–172.
[15] A. Corma, V. Pedro, L. Fernández, Structural incorporation of nitrogen into zeolites and alpos: Ab initio molecular orbital calculations on stability and basicity, Journal of Molecular Catalysis A – Chemical 133 (3) (1998) 241–250.
[16] R. Astala, S.M. Auerbach, The properties of methylene- and amine-substituted zeolites from first principles, Journal of the American Chemical Society 126 (6) (2004) 1843–1848.
[17] D. Lesthaeghe, V. Van Speybroeck, M. Waroquier, Efficient use of bifunctional acid–base properties for alkylammonium formation in amine-substituted zeolites, Journal of the American Chemical Society 126 (30) (2004) 9162–9163.
[18] D. Lesthaeghe, V. Van Speybroeck, G.B. Marin, M. Waroquier, DFT investigation of alkoxide vs. alkylammonium formation in amine-substituted zeolites, Journal of Physical Chemistry B 109 (16) (2005) 7952–7960.
[19] K. Hemelsoet, D. Lesthaeghe, V. Van Speybroeck, M. Waroquier, Bifunctional acid–base catalyzed reactions in zeolites from the HSAB viewpoint, Chemical Physics Letters 419 (1–3) (2006) 10–15.
[20] R. Astala, S.M. Auerbach, P.A. Monson, Density functional theory study of silica zeolite structures: stabilities mechanical properties of SOD, LTA, CHA, MOR and MFI, Journal of Physical Chemistry B 108 (26) (2004) 9208–9215.
[21] J.T. Fermann, T. Moniz, O. Kiowski, T.J. McIntire, S.M. Auerbach, T. Vreven, M.J. Frisch, Modeling proton transfer in zeolites: convergence behavior of embedded and constrained cluster calculations, Journal of Chemical Theory and Computation 1 (6) (2005) 1232–1239.
[22] H. Jónsson, G. Mills, K.W. Jacobsen, Nudged elastic band method for finding minimum energy paths of transitions, in: B.J. Berne, G. Cicotti, D.F. Coker (Eds.), Classical and Quantum Dynamics in Condensed Phase Simulations, World Scientific, Singapore, 1998, pp. 385–404.
[23] Vienna Ab Initio Software Package, developed at Institüt für Materialphysik,Universität Vienna, <http://cms.mpi.univie.ac.at/vasp/>.
[24] H. van Koningsveld, J.C. Jansen, H. van Bekkum, The monoclinic framework structure of zeolite H-ZSM-5 – comparison with the orthorhombic framework of as-synthesized ZSM-5, Zeolites 10 (4) (1990) 235–242.
[25] H. van Koningsveld, High-temperature (350-K) orthorhombic framework structure af zeolite H-ZSM-5, Acta Crystallographica Section B-Structural Science 46 (Part 6) (1990) 731–735.
[26] D.H. Olson, G.T. Kokotailo, S.L. Lawton, W.M. Meier, Crystal-structure and structure-related properties of ZSM-5, Journal of Physical Chemistry 85 (15) (1981) 2238–2243.
[27] J.A. Hriljac, M.M. Eddy, A.K. Cheetham, J.A. Donohue, G.J. Ray, Powder neutron-diffraction and Si-29 MAS NMR-studies of siliceous Zeolite-Y, Journal of Solid State Chemistry 106 (1) (1993) 66–72.
[28] K. Morokuma, S. Dapprich, I. Komaromi, R.D. Froese, M. Holthausen, D.G. Musaev, S. Byun, S. Khoroshun, New implementation of the ONIOM method and its applications to various chemical reactions and structures, Abstracts of Papers of the American Chemical Society 214 (Part 1) (1997) 74COMP.
[29] K. Morokuma, R.D. Froese, S. Dapprich, I. Komaromi, D. Khoroshun, S. Byun, D.G. Musaev, C.L. Emerson, The ONIOM (our own integrated *n*-layered molecular orbital and molecular mechanics) method, and its applications to calculations of large molecular systems, Abstracts of Papers of the American Chemical Society 215 (Part 2) (1998) U218.
[30] S. Dapprich, I. Komaromi, K.S. Byun, K. Morokuma, M.J. Frisch, A new ONIOM implementation in Gaussian98. Part I. The calculation of energies, gradients, vibrational frequencies and electric field derivatives, Journal of Molecular Structure-Theochem. 462 (1999) 1–21.
[31] T. Vreven, K. Morokuma, O. Farkas, H.B. Schlegel, M.J. Frisch, Geometry optimization with QM/MM, ONIOM, and other combined methods. I. Microiterations and constraints, Journal of Computational Chemistry 24 (6) (2003) 760–769.
[32] K. Morokuma, ONIOM and its applications to material chemistry and catalyses, Bulletin of the Korean Chemical Society 24 (6) (2003) 797–801, 10th Korea/Japan Joint Symposium on Theoretical/Computational Chemistry Moleular Structure, Properties and Design, Pohang, South Korea, January 12–15, 2003.
[33] A.D. Becke, Density-Functional thermochemistry. 3. The role of exact exchange, Journal of Chemical Physics 98 (7) (1993) 5648–5652.
[34] C.T. Lee, W.T. Yang, R.G. Parr, Development of the Colle-Salvetti correlation-energy formula into a functional of the electron-density, Physical Review B 37 (2) (1988) 785–789.
[35] R. Krishnan, J.S. Binkley, R. Seeger, J.A. Pople, Self-Consistent molecular-orbital methods. 20. Basis set for correlated wave-functions, Journal of Chemical Physics 72 (1) (1980) 650–654.
[36] M.P. Andersson, P. Uvdal, New scale factors for harmonic vibrational frequencies using the B3LYP density functional method with the triple-ζ basis set 6-311+g(d,p), Journal of Physical Chemistry A 109 (12) (2005) 2937–2941.
[37] J.T. Fermann, C. Blanco, S.M. Auerbach, Modeling proton mobility in acidic zeolite clusters. I. Convergence of transition state parameters from quantum chemistry, Journal of Chemical Physics 112 (15) (2000) 6779–6786.
[38] A.K. Rappé, C.J. Casewit, K.S. Colwell, W.A. Goddard, W.M. Skiff, UFF, a full periodic-table force-field for molecular mechanics and molecular-dynamics simulations, Journal of the American Chemical Society 114 (25) (1992) 10024–10035.
[39] J. Sauer, M. Sierka, Combining quantum mechanics and interatomic potential functions in ab initio studies of extended systems, Journal of Computational Chemistry 21 (16) (2000) 1470–1493.
[40] T. Vreven, M.J. Frisch, K.N. Kudin, H.B. Schlegel, K. Morokuma, Geometry optimization with QM/MM methods II: explicit quadratic coupling, Molecular Physics 104 (5–7) (2006) 701–714.
[41] T. Vreven, K.S. Byun, I. Komaromi, S. Dapprich, J.A. Montgomery, K. Morokuma, M.J. Frisch, Combining quantum mechanics methods with molecular mechanics methods in ONIOM, Journal of Chemical Theory and Computation 2 (3) (2006) 815–826.
[42] H.B. Schlegel, Optimization of equilibrium geometries and transition structures, Journal of Computational Chemistry 3 (2) (1982) 214–218.
[43] W.J. Hehre, R. Ditchfie, J.A. Pople, Self-consistent molecular-orbital methods. 12. Further extensions of gaussian-type basis sets for use in molecular-orbital studies of organic-molecules, Journal of Chemical Physics 56 (5) (1972) 2257.
[44] P.C. Harihara, J.A. Pople, Influence of polarization functions on molecular-orbital hydrogenation energies, Theoretica Chimica Acta 28 (3) (1973) 213–222.
[45] G. Henkelman, H. Jónsson, Improved tangent estimate in the nudged elastic band method for finding minimum energy paths and saddle points, Journal of Chemical Physics 113 (22) (2000) 9978–9985.
[46] G. Henkelman, B.P. Uberuaga, H. Jónsson, A climbing image nudged elastic band method for finding saddle points and minimum energy paths, Journal of Chemical Physics 113 (22) (2000) 9901–9904.
[47] M.J. Frisch, et al., Gaussian Development Version, Revision D.02.
[48] S. Bordiga, A. Damin, F. Bonino, A. Zecchina, G. Spano, F. Rivetti, V. Bolis, C. Prestipino, C. Lamberti, Effect of interaction with H2O and NH3 on the vibrational, electronic, and energetic peculiarities of Ti(IV) centers TS-1 catalysts: a spectroscopic and computational study, Journal of Physical Chemistry B 106 (38) (2002) 9892–9905.
[49] E.M. Flanigen, J.M. Bennett, R.W. Grose, J.P. Cohen, R.L. Patton, R.M. Kirchner, J.V. Smith, Silicalite, a new hydrophobic crystalline silica molecular-sieve, Nature 271 (5645) (1978) 512–516.
[50] A. Giaya, R.W. Thompson, Single-component gas phase adsorption and desorption studies using a tapered element oscillating microbalance, Microporous and Mesoporous Materials 55 (3) (2002) 265–274.
[51] V. Gutmann, The Donor–Acceptor Approach to Molecular Interactions, Plenum Press, New York, 1978.
[52] M.G. Voronkov, V.P. Mileshkevich, Y.A. Yuzhelevskii, Complexes of organosilicon compounds, having siloxane bond, Uspekhi Khimii 45 (12) (1976) 2253–2273.
[53] H. Koller, A. Wolker, L.A. Villaescusa, M.J. Díaz-Cabañas, S. Valencia, M.A. Camblor, Five-coordinate silicon in high-silica zeolites, Journal of the American Chemical Society 121 (14) (1999) 3368–3376.
[54] I.V. Mishin, T.R. Brueva, G.I. Kapustin, Heats of adsorption of ammonia and correlation of activity and acidity in heterogeneous catalysis, Adsorption-Journal of the International Adsorption Society 11 (3–4) (2005) 415–424.
[55] K. Tsutsumi, Y. Mitani, H. Takahashi, Direct measurement of the interaction energy between solids and gases. 9. Heats of adsorption of ammonia and pyridine on several solids at high-temperature, Bulletin of the Chemical Society of Japan 56 (7) (1983) 1912–1916.
[56] A. Auroux, J.C. Vedrine, Microcalorimetric characterization of acidity and basicity of various metallic oxides, in: B. Imelik, C. Naccache, G. Coudurier, Y. Ben Taarit, J.C. Vedrine (Eds.), Catalysis by Acids and Bases, Studies in Surface Science and Catalysis, vol. 20, 1985, pp. 311–318.
[57] U. Viswanathan, J.T. Fermann, L.K. Toy, S.M. Auerbach, T. Vreven, M.J. Frisch, Modeling proton jumps in HY zeolite: effects of acid site heterogeneity, Journal of Physical Chemistry C 111 (49) (2007) 18341–18347.
[58] E.H. Teunissen, F.B. van Duijneveldt, R.A. van Santen, Interaction of NH_3 with a zeolitic proton – Ab initio quantum-chemical cluster calculations, Journal of Physical Chemistry 96 (1) (1992) 366–371.

[59] E.H. Teunissen, R.A. van Santen, A.P.J. Jansen, F.B. van Duijneveldt, NH_4^+ in zeolites – coordination and solvation effects, Journal of Physical Chemistry 97 (1) (1993) 203–210.
[60] S.P. Greatbanks, P. Sherwood, I.H. Hillier, R.J. Hall, N.A. Burton, I.R. Gould, Adsorption energies of NH_3 and NH_4^+ in zeolites – an embedded-cluster model including electron correlation, Chemical Physics Letters 234 (4–6) (1995) 367–372.
[61] M. Brandle, J. Sauer, Combining ab initio techniques with analytical potential functions.A study of zeolite–adsorbate interactions for NH_3 on H-faujasite, Journal of Molecular Catalysis A – Chemical 119 (1–3) (1997) 19–33.
[62] D.R. Alfonso, K.D. Jordan, A flexible nudged elastic band program for optimization of minimum energy pathways using ab initio electronic structure methods, Journal of Computational Chemistry 24 (8) (2003) 990–996.
[63] G. Kresse, J. Furthmuller, Efficient iterative schemes for ab initio total-energy calculations using a plane-wave basis set, Physical Review B 54 (16) (1996) 11169–11186.
[64] G.P. Srivastava, Broyden method for self-consistent field convergence acceleration, Journal of Physics A – Mathematical and General 17 (6) (1984) L317–L321.